Submitted to The Astrophysical Journal January 5, 2012
Preprint typeset using LaTeX style emulateapj v. 11/10/09

arXiv:1201.0991v1 [astro-ph.CO] 4 Jan 2012

THE ATACAMA COSMOLOGY TELESCOPE: DYNAMICAL MASSES AND SCALING RELATIONS FOR A SAMPLE OF MASSIVE SUNYAEV-ZEL'DOVICH EFFECT SELECTED GALAXY CLUSTERS

Cristóbal Sifón[1,†,††,‡], Felipe Menanteau[2,‡], Matthew Hasselfield[3], Tobias A. Marriage[4], John P. Hughes[2,‡], L. Felipe Barrientos[1], Jorge González[1], Leopoldo Infante[1], Graeme E. Addison[5], Andrew J. Baker[2], Nick Battaglia[6], J. Richard Bond[6], Sudeep Das[7], Mark J. Devlin[8], Joanna Dunkley[5], Rolando Dünner[1], Megan B. Gralla[4], Amir Hajian[6], Matt Hilton[9], Adam D. Hincks[10], Arthur B. Kosowsky[11], Danica Marsden[12], Kavilan Moodley[13], Michael D. Niemack[14], Michael R. Nolta[6], Lyman A. Page[10], Bruce Partridge[15], Erik D. Reese[8], Neelima Sehgal[16], Jon Sievers[6], David N. Spergel[16], Suzanne T. Staggs[10], Robert J. Thornton, Jr.[17,8], Hy Trac[18], Edward Wollack[19]

[1]Departamento de Astronomía y Astrofísica, Facultad de Física, Pontificia Universidad Católica de Chile, Casilla 306, Santiago 22, Chile
[2]Rutgers University, Department of Physics & Astronomy, 136 Frelinghuysen Rd, Piscataway, NJ 08854, USA
[3]Department of Physics and Astronomy, University of British Columbia, Vancouver, BC V6T 1Z4, Canada
[4]Department of Physics and Astronomy, The Johns Hopkins University, Baltimore, Maryland 21218-2686, USA
[5]Sub-department of Astrophysics, University of Oxford, Denys Wilkinson Building, Keble Road, Oxford OX1 3RH, UK
[6]Canadian Institute for Theoretical Astrophysics, University of Toronto, Toronto, ON, Canada M5S 3H8
[7]Berkeley Center for Cosmological Physics, LBL and Department of Physics, University of California, Berkeley, CA 94720, USA
[8]University of Pennsylvania, Physics and Astronomy, 209 South 33rd Street, Philadelphia, PA 19104, USA
[9]School of Physics and Astronomy, University of Nottingham, University Park, Nottingham, NG7 2RD, UK
[10]Joseph Henry Laboratories of Physics, Jadwin Hall, Princeton University, Princeton, NJ, 08544, USA
[11]University of Pittsburgh, Physics & Astronomy Department, 100 Allen Hall, 3941 O'Hara Street, Pittsburgh, PA 15260, USA
[12]Department of Physics, University of California-Santa Barbara, Santa Barbara, CA 93106-9530, USA
[13]University of KwaZulu-Natal, Astrophysics & Cosmology Research Unit, School of Mathematical Sciences, Durban, 4041, South Africa.
[14]NIST Quantum Devices Group, 325 Broadway Mailcode 817.03, Boulder CO, USA 80305
[15]Department of Physics and Astronomy, Haverford College, Haverford, PA 19041, USA
[16]Department of Astrophysical Sciences, Peyton Hall, Princeton University, Princeton, NJ, 08544, USA
[17]Department of Physics, West Chester University, West Chester, PA 19383, USA
[18]Department of Physics, Carnegie Mellon University, Pittsburgh, PA 15213, USA and
[19]Code 553/665, NASA/Goddard Space Flight Center, Greenbelt, Maryland, 20771, USA

Submitted to The Astrophysical Journal January 5, 2012

ABSTRACT

We present the first dynamical mass estimates and scaling relations for a sample of Sunyaev-Zel'dovich effect (SZE) selected galaxy clusters. The sample consists of 16 massive clusters detected with the Atacama Cosmology Telescope (ACT) over a 455 deg^2 area of the southern sky. Deep multi-object spectroscopic observations were taken to secure intermediate-resolution ($R \sim 700-800$) spectra and redshifts for ≈ 60 member galaxies on average per cluster. The dynamical masses M_{200c} of the clusters have been calculated using simulation-based scaling relations between velocity dispersion and mass. The sample has a median redshift $z = 0.50$ and a median mass $M_{200c} \simeq 11 \times 10^{14}\, h_{70}^{-1} M_\odot$ with a lower limit $M_{200c} \simeq 5 \times 10^{14}\, h_{70}^{-1} M_\odot$, consistent with the expectations for the ACT southern sky survey. These masses are compared to the ACT SZE properties of the sample, specifically, the central SZE amplitude y_0, the Compton signal within a $0.5'$ pixel $y_{0'.5}$, and the integrated Compton signal Y_{200c}, which we use to derive SZE-Mass scaling relations. All SZE estimators correlate with dynamical mass with low intrinsic scatter (11% - 16%), in agreement with numerical simulations. The influence of dynamically disturbed clusters on these scaling relations is also considered. Using the 3-dimensional information available, we divide the sample into relaxed and disturbed clusters and find that $\sim 50\%$ of the clusters are disturbed. We conclude that disturbed systems do not significantly bias the scaling relations but might modestly boost their scatter.

Subject headings: galaxy clusters: general, redshifts — galaxy clusters: dynamics, masses — SZ effect: scaling relations

1. INTRODUCTION

Studies of clusters of galaxies have had a wide impact on our understanding of galaxy formation and cosmology (see Voit 2005, for a review). They are a unique laboratory for studying the effects of the environment (high density, gas pressure, collisions, etc.) on galaxy evolution (Butcher & Oemler 1984; Balogh et al. 1999; Hansen et al. 2009). At the same time, number counts of galaxy clusters, sensitive to the amplitude of matter fluctuations, can provide constraints on various cosmological parameters (Bahcall & Fan 1998; Evrard et al. 2002; Vikhlinin et al. 2009; Mantz et al. 2010b,c; Rozo et al. 2010). An accurate determination of the latter requires that we know the mass and redshift distributions of

---

[†] Based in part on observations collected at the European Organisation for Astronomical Research in the Southern Hemisphere, Chile, under programs 084.A-0577 and 086.A-0425.

[††] Based in part on observations obtained at the Gemini Observatory, which is operated by the Association of Universities for Research in Astronomy, Inc., under a cooperative agreement with the NSF on behalf of the Gemini partnership: the National Science Foundation (United States), the Science and Technology Facilities Council (United Kingdom), the National Research Council (Canada), CONICYT (Chile), the Australian Research Council (Australia), Ministério da Ciência e Tecnologia (Brazil) and Ministerio de Ciencia, Tecnología e Innovación Productiva (Argentina).

[‡] Visiting astronomer, Gemini South Observatory.

clusters with good precision.

The Sunyaev-Zel'dovich Effect (SZE; Zel'dovich & Sunyaev 1969; Sunyaev & Zel'dovich 1970) is a distortion in the Cosmic Microwave Background (CMB) temperature produced by inverse-Compton scattering of CMB photons as they interact with the hot electrons of the intracluster medium (ICM) of a galaxy cluster. Its surface brightness is independent of redshift, and its strength is proportional to the line-of-sight column density times the electron temperature. The SZE is a powerful tool for detecting massive clusters to high redshifts (see, e.g., the reviews by Birkinshaw 1999; Carlstrom et al. 2002).

Early measurements of the SZE were achieved with targeted observations of known clusters. These revealed the power of SZE studies, reaching from gas physics and inner structure of clusters (Grego et al. 2001; Benson et al. 2004), to cosmological parameters such as the Hubble constant (Birkinshaw et al. 1991; Hughes & Birkinshaw 1998) and the energy density of matter in the universe, Ω_M (Grego et al. 2001). Large SZE surveys over cosmologically significant areas of the sky have recently come to fruition as the Atacama Cosmology Telescope (ACT, Fowler et al. 2007; Swetz et al. 2011) and the South Pole Telescope (SPT, Carlstrom et al. 2009) have begun scanning large areas of the sky at millimeter wavelengths. The Planck satellite (Tauber et al. 2010) is conducting an all-sky survey and has recently released the first all-sky sample of SZE-selected galaxy clusters (Planck Collaboration 2011a). The first cluster detections with ACT and SPT are presented in Hincks et al. (2010) and Staniszewski et al. (2009), respectively.

The rapidly growing SZE cluster samples have the potential to place strong constraints on cosmological parameters (e.g., Battye & Weller 2003). Both numerical simulations (Springel et al. 2001a; da Silva et al. 2004; Motl et al. 2005; Nagai 2006; Battaglia et al. 2011) and analytical studies (Reid & Spergel 2006; Ashfordi 2008; Shaw et al. 2008) suggest a tight correlation between cluster mass and SZE signal. On the other hand, biased mass estimates can have a large impact on cosmological parameter determination (e.g., Francis et al. 2005). By limiting their study to the high-significance clusters, Sehgal et al. (2011) have shown the power of the ACT sample in constraining cosmological parameters, particularly the dark energy equation-of-state parameter w and the root-mean-square (RMS) mass fluctuations on a scale of $8\,h^{-1}\,\mathrm{Mpc}$, σ_8. Likewise, Vanderlinde et al. (2010) have used SPT data to set cosmological constraints, with similar findings. They have also shown that these improvements can be achieved only in the presence of a well-calibrated scaling relation between mass and SZE signal. To assess the scaling of SZE signal with mass, independent means of measuring the mass are crucial.

Benson et al. (2011) used X-ray observations in combination with SZE measurements to derive an empirical scaling relation between mass and SZE signal. This allowed them to confirm that SZE-selected samples of clusters yield significant improvements when added to other datasets to constrain cosmological parameters. While X-ray observations have proven to be an effective way of measuring cluster masses, and have been exploited to characterize the SZE signal (LaRoque et al. 2006; Bonamente et al. 2008; Andersson et al. 2011; Melin et al. 2011; Planck Collaboration 2011b), they are do not provide truly independent mass estimates from SZE measurements, since both rely on the properties of the gas in the ICM and should be affected by similar physics.

The velocity dispersion of cluster member galaxies is one of the most widely used methods for constraining cluster mass, and is independent of the properties of the gas in the ICM. It takes into account the galaxy distribution and relies, to some extent, on the assumption that the clusters are relaxed (i.e., virialized). Until recently, however, mass measurements to independently calibrate the SZE signal with mass have come from optical richness (Menanteau & Hughes 2009; High et al. 2010; Menanteau et al. 2010a; Planck Collaboration 2011c) and lensing analyses (Sealfon et al. 2006; Umetsu et al. 2009; Marrone et al. 2011). Hand et al. (2011) presented stacked ACT data in the directions of Luminous Red Galaxies (LRGs) from the Sloan Digital Sky Survey (SDSS) Data Release 7 (DR7, Abazajian et al. 2009) using optical luminosity–based masses. This approach allowed them to probe the SZE signal from lower mass systems than otherwise possible.

Rines et al. (2010) presented the first statistical comparison between dynamically-estimated masses and integrated SZE signal from a sample of 15 nearby ($z < 0.3$) galaxy clusters, showing that masses thus determined and the integrated SZE flux are correlated at the $\approx 99\%$ confidence level. Furthermore, they estimate that the significance is higher than that of the correlation between SZE and weak lensing masses from Marrone et al. (2009), probably because of the small apertures used in the latter study. However, since their sample was not homogeneously selected, Rines et al. (2010) do not account for observational biases in their sample and do not report a formal scaling relation between mass and SZE flux.

In this work we present spectroscopic redshifts and—for the first time—dynamical masses of a sample of clusters of galaxies selected with the SZE. These clusters were observed by ACT in its 2008 southern sky survey at 148 GHz (Marriage et al. 2011a), and were optically confirmed by Menanteau et al. (2010b). We use a variety of SZE diagnostics to assess the scaling with dynamical mass and thus present the first robust scaling relations between dynamical masses and SZE signal for a sample of SZE selected clusters.

Throughout this work we use a flat ΛCDM cosmology consistent with WMAP-7 data (Komatsu et al. 2011), with $\Omega_\Lambda = 0.73$, $\Omega_M = 0.27$ and $H_0 = 70h_{70}\,\mathrm{km\,s^{-1}\,Mpc^{-1}}$. Masses and integrated SZE signals are estimated within a radius r_{200c} which encloses a density 200 times the critical density of the Universe at the redshift of the cluster, $\rho_c(z) = 3H^2(z)/8\pi G$. All quoted errors are 68% confidence intervals unless otherwise stated.

2. OBSERVATIONS

2.1. *ACT SZE Observations*

ACT is a six-meter off-axis Gregorian telescope operating at an altitude of 5200 m in the Atacama Desert in Chile, designed to observe the CMB at arcminute-scale resolution. It has three 1024-element arrays of transition edge sensors operating at 148, 218 and 277 GHz. ACT began observing in late 2007, and surveyed two regions in the sky with a total area of 755 deg^2 (Marriage et al. 2011b; Hasselfield et al. 2012, in prep.). The processes of cluster detection and extraction are thoroughly described in Marriage et al. (2011a, and references therein). In short, the maps are match-filtered and convolved with a beta-model profile with $\beta = 0.86$ with varying core radius θ_c from $0\farcm25$ to $4\farcm0$. Cluster signal-to-noise ratio (S/N) is measured as the maximum S/N from this set of filtered maps.

We report on a large spectroscopic follow-up campaign of an ACT 148 GHz cluster sample, which was obtained from a 455 sq. deg. survey of the southern sky. The survey is roughly bounded by right ascensions $00^{\mathrm{h}}12^{\mathrm{m}}$ and $07^{\mathrm{h}}08^{\mathrm{m}}$ and declinations $-56^{\circ}11'$ and $-49^{\circ}00'$. For further details on the ACT observations, data reduction, and cluster detection procedure, see Fowler et al. (2010); Marriage et al. (2011a).

2.1.1. *The Cluster Sample*

In this study we consider a total of 19 clusters, spanning a wide range in mass and redshift. We focus, in particular, on the subsample of 16 that were detected by ACT through their SZ signal. This subsample contains 15 systems that were detected by ACT in the 2008 single-season maps (Marriage et al. 2011a) and confirmed optically on 4m-class telescopes (Menanteau et al. 2010b), plus one additional cluster (ACT-CL J0521–5104) detected in the new analysis of multi-season maps (Hasselfield et al. 2012, in prep.). This latter cluster was initially targeted for spectroscopic follow-up based on its optical richness alone (Menanteau et al. 2010a). These 16 clusters were selected based on a redshift cut of $z_{\mathrm{phot}} > 0.35$ and were all discovered with the SZE, with the exceptions of ACT-CL J0330–5227 (X-rays, Werner et al. 2007) and ACT-CL J0521–5104 (optical, Menanteau et al. 2010a). ACT-CL J0330–5227 is located 12′ North-East (NE) of Abell 3128 ($z = 0.06$; Colless & Hewett 1987; Katgert et al. 1996), but Werner et al. (2007) found it to be an unrelated, background cluster at $z = 0.44$ based on the observed energy of the Fe K X-ray emission line using *XMM-Newton* observations and the optical spectrum of the Brightest Cluster Galaxy (BCG). Hincks et al. (2010) have shown that the observed SZE signal is clearly related to the background cluster. Four clusters were initially reported by SPT (Staniszewski et al. 2009; Vanderlinde et al. 2010, see §6.1) and studied optically by Menanteau et al. (2010a). ACT-CL J0546–5345 is the only cluster with a dynamical mass estimate prior to this study (Brodwin et al. 2010, see §6.1.9).

Of the 16 ACT clusters, 10 are newly discovered. Menanteau et al. (2010b) confirmed them as clusters with a BCG and an accompanying red sequence of galaxies and studied their X-ray properties from archival *ROSAT* data for the 15 clusters, plus *Chandra* and/or *XMM-Newton* data when available. The clusters cover the range $\sim 1-30\times10^{44}\,\mathrm{erg\,s^{-1}}$ in X-ray luminosity as measured in the $0.1-2.4$ keV band. Photometric redshifts were estimated for these 15 clusters by Menanteau et al. (2010b). The spectroscopic redshift range covered by the sample is $0.28 < z < 1.07$ with a median redshift $z = 0.50$.

Additionally, we report on three optically selected, high-richness galaxy clusters from the Southern Cosmology Survey (SCS; Menanteau et al. 2010a). These clusters were part of our 2009B follow-up observations before the ACT maps were available for cluster detection, and were not detected by ACT. They are briefly discussed in §6.2.

2.1.2. *Cluster SZE Measurements*

To characterize the SZE produced by each cluster (in the 148 GHz band) we study three different estimators, corresponding to different map filters and different apertures for extracting the SZE signal. The values for the sample are listed in Table 1.

The first estimator was introduced by Sehgal et al. (2011) and corresponds to the SZE signal of the brightest $0'.5$ pixel in a map match-filtered with a Gaussian profile of fixed $2'$ FWHM. This estimator is referred to as $y_{0'.5}$ hereafter. We use the values of $y_{0'.5}$ from Sehgal et al. (2011), which have been measured using data from the 2008 observations only.

Table 1
ACT-SZE Measurements of Clusters

Cluster	z	$y_{0'.5}$ [a] $\times10^{-4}$	y_0 $\times10^{-4}$	Y_{200c} $\times10^{-10}$
ACT-CL J0102–4915	0.870	1.80 ± 0.22	3.50 ± 0.43	6.38 ± 0.76
ACT-CL J0215–5212	0.480	0.99 ± 0.22	0.79 ± 0.18	1.62 ± 0.41
ACT-CL J0232–5257	0.556	0.99 ± 0.22	0.61 ± 0.17	1.23 ± 0.30
ACT-CL J0235–5121	0.278	1.03 ± 0.22	0.97 ± 0.19	4.22 ± 0.89
ACT-CL J0237–4939	0.334	0.73 ± 0.22	0.93 ± 0.26	4.62 ± 1.33
ACT-CL J0304–4921	0.392	0.88 ± 0.22	1.51 ± 0.31	4.55 ± 1.08
ACT-CL J0330–5227	0.442	1.39 ± 0.22	1.23 ± 0.18	3.92 ± 0.58
ACT-CL J0346–5438	0.530	0.88 ± 0.22	1.04 ± 0.22	2.01 ± 0.49
ACT-CL J0438–5419	0.421	1.54 ± 0.22	1.62 ± 0.13	4.93 ± 0.44
ACT-CL J0509–5341	0.461	1.03 ± 0.22	0.41 ± 0.13	0.51 ± 0.22
ACT-CL J0521–5104	0.675	0.59 ± 0.22	0.71 ± 0.16	1.23 ± 0.29
ACT-CL J0528–5259	0.768	0.73 ± 0.22	0.49 ± 0.13	0.44 ± 0.15
ACT-CL J0546–5345	1.066	1.14 ± 0.22	0.91 ± 0.14	1.15 ± 0.14
ACT-CL J0559–5249	0.609	0.81 ± 0.22	0.89 ± 0.14	2.23 ± 0.26
ACT-CL J0616–5227	0.684	1.32 ± 0.22	1.00 ± 0.15	2.04 ± 0.22
ACT-CL J0707–5522	0.296	0.77 ± 0.22	0.54 ± 0.21	2.48 ± 0.56

Note. — Redshifts are listed for reference. See Table 3 for details.
[a] Measurements using 2008 ACT data only. Uncertainties correspond to the RMS scatter in $y_{\mathrm{recovered}}-y_{\mathrm{true}}$ from simulations; see Sehgal et al. (2011).

We also consider the dimensionless, matched filter SZE amplitude, which we denote as y_0. The analysis used to derive these values is presented in Hasselfield et al. (2012, in prep.); it is similar to that performed by Marriage et al. (2011a) but now includes the multi-season (2008-2010) ACT observations. In brief, the ACT map is filtered optimally to extract the amplitude of the temperature decrement of clusters modeled by the generalized Navarro-Frenk-White (NFW, Navarro et al. 1995) best-fit profile of Arnaud et al. (2010)—hereafter "the A10 profile"—with a fixed FWHM of $2'$. The corresponding temperature decrement, δT, is scaled to y_0 using the standard non-relativistic SZE frequency dependence (Sunyaev & Zel'dovich 1980). Our new y_0 measurements correlate well with $y_{0'.5}$, with a Pearson's r-value of 0.75.

The previous two SZE estimators can be used without any prior knowledge of the properties of the clusters to be detected in a large survey area. Hence, determining the mass scaling laws for these estimators is essential for cosmological studies based on the abundance of massive clusters. Once the redshift of the cluster is known, an integrated Compton signal $Y = \int y d\Omega$ can be measured for each cluster within a physical radius. Larger integration areas tend to give measurements that are more robust against the effects of cluster physics such as AGN feedback (Motl et al. 2005; Nagai 2006; Reid & Spergel 2006), and to projection effects (Shaw et al. 2008). Velocity dispersion–mass scalings are usually measured at r_{200c} (see Eq. 1). The dynamical information therefore yields a measurement of the size of the cluster, which is used in the calculation of Y_{200c}. We use the same match-filtered map as for the extraction of y_0, and the A10 profile to extract each cluster's spherical Y value from within r_{200c}.

2.2. *Optical Spectroscopy*

Table 2
Spectroscopic Observation Details

Run	Semester	PI	Tel./Inst.	Program ID	Mode	Grating	Hours	N_{cl}
1	2009B	Infante	VLT/FORS2	084.A-0577	Service	GRIS 300I+11	14	3
2	2009B	Barrientos	Gemini-S/GMOS	GS-2009B-Q-2	Service	R400_G5325	20	4
3	2010B	Infante	VLT/FORS2	086.A-0425	Service	GRIS 300I+11	15	2
4	2010B	Barrientos/Menanteau [a]	Gemini-S/GMOS	GS-2010B-C-2	Classical	R400_G5325	40	10

Note. — N_{cl} is the number of clusters observed in each run. Each cluster was fully observed in one run.

[a] Joint Chile/US proposal

The spectroscopic observations were carried out in two semesters, 2009B and 2010B. Each semester was split into two observing runs, one with FORS2 at the VLT (Appenzeller et al. 1998) and one with GMOS at Gemini South (Hook et al. 2004), both telescopes located in Chile. The details of each observing run are listed in Table 2. In total, we had 89 hours of observation, during which we collected Multi-Object Spectroscopy for 19 clusters.

Targets were selected by a two-step process. First, a photometric redshift–selected catalog was constructed, including galaxies within ± 0.1 of the redshift of the BCG. Within this catalog, galaxies were visually selected based on their *gri* colors, with preference given to bright galaxies. All our spectroscopic observations cover the wavelength range $\sim 4000-8000$Å. In this range several spectral features are observable at the median photometric redshift of 0.54 (Menanteau et al. 2010b). These are mainly the CaII K-H absorption doublet (at rest-frame wavelength $\lambda_0 \sim 3950$Å), which is the spectral signature of elliptical galaxies, plus other absorption lines such as the G-band ($\lambda_0 = 4300$Å), Hβ ($\lambda_0 = 4861$Å) and the MgII-triplet ($\lambda_0 \sim 5175$Å), plus the [OII] emission line at rest-frame λ_0 = 3727Å. The NaI absorption-doublet ($\lambda_0 \sim 5892$Å) is also observable in the low-z clusters.

2.2.1. *VLT-FORS2 Observations*

The FORS2-2009B observations (Run 1) were aimed at newly SZE-detected clusters regarded as "secure" candidates detected with ACT in 2008. These clusters had already been reported by Staniszewski et al. (2009) as SZE detections and their physical properties characterized in Menanteau & Hughes (2009).

Run 3 was mostly focused on getting detailed information for ACT-CL J0102–4915 ("El Gordo," Menanteau et al. 2011), which was detected as the largest decrement in the ACT maps. ACT-CL J0559–5249 was also included in this run.

Runs 1 and 3 were executed in Service Mode in semesters 2009B and 2010B, respectively. The instrument setup in both runs was the same, using the GRIS 300I+11 grism and $1''$–wide slits, which provides a resolving power $R = 660$ at $\lambda =$ 8600Å. A total of 18 FORS2/MXU masks were observed for the five clusters. Each mask was observed for 40 min, which we estimated to be the best compromise between maximizing S/N and number of masks.

FORS2 has a field of view of $6'.8 \times 6'.8$ in the standard resolution setup, which corresponds to a width of 2517 h_{70}^{-1} kpc at $z = 0.5$.

2.2.2. *Gemini-GMOS Observations*

The GMOS-2009B observations (Run 2) were aimed at four optically selected clusters from the SCS whose richness-based mass estimates suggested that they would be detected by ACT in the SZE survey (Menanteau et al. 2010a). However, as mentioned above, only one object was in fact detected by ACT (ACT-CL J0521–5104); the other three are discussed in §6.2. The total integration time per mask was 3600 s (2×1800 s). Two exposures at slightly different central wavelengths per mask were required to cover the two 37-pixel gaps between the CCDs which run across the dispersion axis.

Targets for Run 4 (GMOS-2010B) were selected from the sample of clusters newly discovered by ACT presented in Marriage et al. (2011a) and optically confirmed by Menanteau et al. (2010b). Run 4 was the only one executed in Classical Mode, during five consecutive nights (Dec. 6-10), all with clear, photometric conditions and seeing $\lesssim 0.8''$. Based on our experience in Run 2 we decided to reduce the integration time to 2400 s (2×1200s) for each mask during Run 4. This, coupled with a $\sim 20\%$ higher efficiency than Queue Mode, allowed us to observe a larger number of masks (and clusters) while still obtaining the necessary S/N in the relevant spectral lines.

In both GMOS runs we used the R400_G5325 grating and $1''$-wide slits, providing a resolving power of $R \sim 800$ with a 2x2 binning at $\lambda \sim 7000$Å. In the standard setup GMOS has a field of view of $5'.5 \times 5'.5$ (2036 h_{70}^{-1} kpc at $z = 0.5$).

2.2.3. *Data Reduction*

We have developed reduction pipelines both for the FORS2 and GMOS data, based on the existing software by ESO and Gemini respectively, which work with IRAF/PyRAF[4]. Cosmic rays are removed using L.A.Cosmic (van Dokkum 2001) with a detection limit of 4.5σ. The wavelength calibrations were done using CuAr lamps in the case of GMOS data and HeAr lamps for VLT data. The sky is subtracted from each spectrum using a constant value determined locally within each slitlet. In the case of GMOS data, the individual exposures are coadded at this point. Finally, the 1-D spectra are extracted from each slit and matched with the input photometric catalogs used to generate the masks.

3. ANALYSIS AND RESULTS

3.1. *Galaxy Redshifts*

Galaxy redshifts are measured by cross-correlating the spectra with galaxy spectral templates of the SDSS DR7 using the RVSAO/XCSAO package for IRAF (Kurtz & Mink 1998); the spectral features in each spectrum have been confirmed with the 2d spectra by visual inspection. We have been able to estimate reliable redshifts for ~ 1200 galaxies which comprise $\sim 80\%$ of all targeted objects.

---

[4] The pipeline used to reduce GMOS data—dubbed "`pygmos`"—is available at **http://www.astro.puc.cl/~cjsifon/pygmos/**.

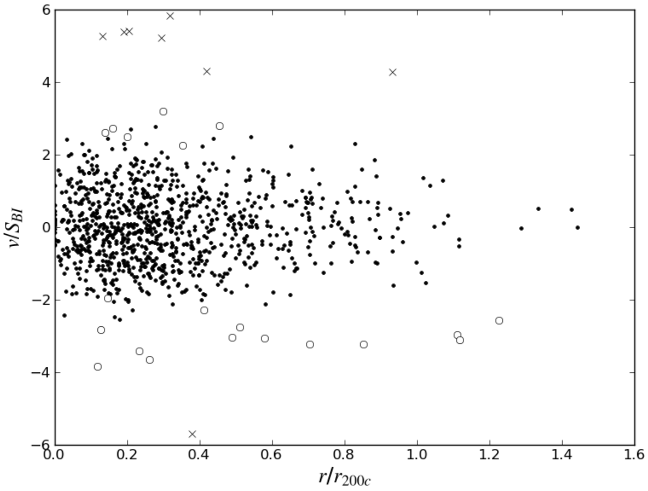

Figure 1. The "stacked" result of the shifting gapper method of member selection, showing the galaxies in all 16 SZE-detected clusters. The horizontal axis shows the cluster-centric distance normalized by r_{200c} for each cluster and the vertical axis shows the peculiar velocity of each galaxy, normalized by the velocity dispersion of the corresponding cluster. Black dots show member galaxies, open circles show galaxies rejected by the method, and crosses show galaxies with peculiar velocities larger than $4000\,\mathrm{km\,s^{-1}}$. Galaxies with peculiar velocities larger than $6S_{BI}$ are not shown for clarity.

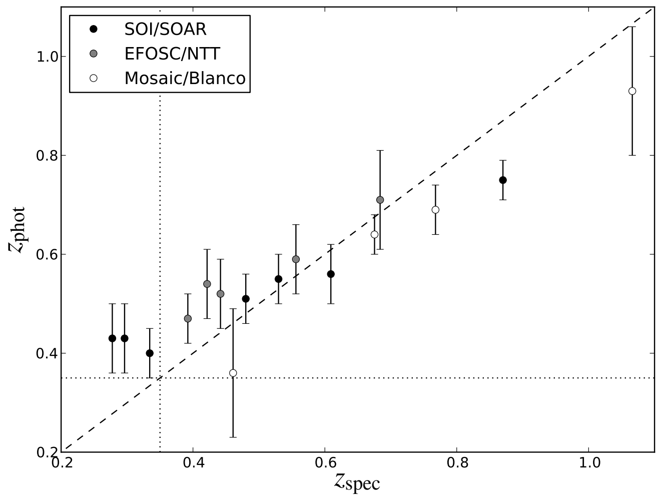

Figure 2. Comparison between spectroscopic redshifts from this work with initial *gri* photometric redshift estimates from Menanteau et al. (2010b). The instruments/telescopes with which each cluster was observed are identified in the legend. The dashed line shows $z_{\rm phot} = z_{\rm spec}$. The dotted horizontal line shows the sample selection cut, $z_{\rm phot} = 0.35$, and the dotted vertical line shows the corresponding $z_{\rm spec} = 0.35$.

The median RMS in the wavelength calibration is ~ 0.3Å and is similar for both instruments. At a central wavelength of 6000 Å, this corresponds to a velocity uncertainty of $15\,\mathrm{km\,s^{-1}}$, which is within the errors of the cross-correlation velocity. In particular, the latter is typically $\Delta(cz) \sim 40-80\,\mathrm{km\,s^{-1}}$, as calculated by RVSAO. It has been established experimentally that the true cross-correlation errors are larger than those reported by RVSAO, by a factor ~ 1.7 (e.g., Quintana et al. 2000), strengthening the point that the calibration errors are well within the velocity measurement errors.

We have included the member catalog for ACT-CL J0546–5345 published by Brodwin et al. (2010). Seven galaxies have been observed both by Brodwin et al. (2010) and by us; all redshifts are consistent within 2σ. We therefore use our measurements for those galaxies in the following analysis.

3.2. *Cluster Redshifts and Velocity Dispersions*

It is of great importance to correctly determine cluster membership to avoid a biased measurement of the velocity dispersion (Beers et al. 1991). This is a complicated problem and many methods have been developed to handle it. In this analysis, membership of galaxies to a cluster is determined by applying a cut in (rest-frame) velocity space of $4000\,\mathrm{km\,s^{-1}}$, and then applying the shifting gapper method (Fadda et al. 1996). To do this, we define annular bins around the BCG, each of which has at least 15 galaxies and radial width $\geq 250\,h_{70}^{-1}\,\mathrm{kpc}$. We consider the histogram of velocities of member galaxies within each bin. We assume the profile is symmetric, and identify the main body of galaxies as those whose velocity is bounded by gaps of $\geq 500\,\mathrm{km\,s^{-1}}$. Following Katgert et al. (1996) and Fadda et al. (1996), galaxies separated from the main body by $\geq 1000\,\mathrm{km\,s^{-1}}$ are considered interlopers and are removed. The selection method is iterated until the number of members is stable. This usually happens after the second iteration. A total of 948 galaxies ($\sim 65\%$ of all targets) have been selected as cluster members. Most of these galaxies show the spectral signatures of elliptical galaxies and do not have emission lines, and only a few emission-line galaxies belong to clusters (see §4.3). The galaxies remaining at this point are considered members of the cluster. Figure 1 shows the "stacked" result of this method, with members as solid dots. The values have been normalized to allow for direct comparison of all clusters. We have explored systematic effects coming from the member selection method by changing the width of the bins, the number of galaxies per bin, and the size of either gap in the shifting gapper. Varying these parameters yields results that are consistent with the reported velocity dispersions.

It is clear from Fig. 1 that, while our sampling extends to r_{200c} in most cases, it is mainly concentrated within the inner $0.8\,r_{200c}$ of the clusters. This is not expected to bias our results since velocity dispersion profiles are, in general, flat from $\sim 0.5r_{200c}$ outwards (Fadda et al. 1996; Biviano & Girardi 2003; Faltenbacher & Diemand 2006). We use the biweight estimators of location (hereafter $z_{\rm BI}$) (Beers et al. 1990) for the redshift of the cluster and scale, $S_{\rm BI}$, for the velocity dispersion. All errors have been estimated with the bootstrap resampling technique with 5000 iterations. The redshifts of the clusters are presented in Fig. 2, where they are compared to the photometric redshifts of Menanteau et al. (2010b). The median redshift of the sample is $z = 0.50$. The slightly biased photometric redshifts apparent on Fig. 2 are mainly due to two factors: the lack of a well-characterized filter response function for the telescopes involved in the imaging follow-up and the use of only three to four filters for the determination of photometric redshifts (Menanteau et al. 2010b).

Danese et al. (1980) showed that the observational errors on the redshifts of galaxies introduce a bias in the measured velocity dispersion. However, for a cluster of $\sim 1 \times 10^{15}\,M_{\odot}$ with individual errors as measured in this work (i.e., $\lesssim 100\,\mathrm{km\,s^{-1}}$), this correction is $< 0.1\%$ (and even lower for more massive clusters), and it is therefore not considered here[5].

---

[5] As mentioned before, the errors calculated by RVSAO are smaller than the true cross-correlation errors. Even so, the Danese et al. (1980) correction

4. DYNAMICAL MASSES

In this section, we use the velocity dispersions measured in the previous section to estimate cluster masses. The dynamical state of each cluster is also studied, including signs of substructure and the fraction and influence of emission-line galaxies in the cluster population. Both factors can, in principle, bias the velocity dispersion and thus the dynamical mass of the cluster. Moreover, they are not expected to be completely independent, since emission-line galaxies are generally newly incorporated galaxies, which might mean recent (or near-future) mergers involving the main cluster (Moore et al. 1999; Book & Benson 2010).

4.1. *Dynamical Mass Estimates*

The relationship between velocity dispersions and masses has been the focus of several studies. As a first-order approach, Heisler et al. (1985) studied simple variations of the virial theorem and found that they all behave similarly, and that it is not possible to distinguish among them. Carlberg et al. (1997) compared masses obtained from the virial theorem to those obtained with the Jeans equation in observed clusters. They found that the former are biased high by a factor of 10-20% and associated this bias with a surface pressure correction factor of the same order.

More recently and based on large cosmological simulations Evrard et al. (2008) concluded that massive ($M_{200c} > 10^{14} M_\odot$) clusters are, on average, consistent with a virialized state, and find a best-fit scaling relation for dark matter halos described by NFW profiles in a variety of cosmologies. Accordingly, the mass enclosed within r_{200c} is

$$M_{200c} = \frac{10^{15}}{0.7 h_{70}(z)} \left(\frac{\sigma_{\rm DM}}{\sigma_{15}} \right)^{1/\alpha} M_\odot \,, \qquad (1)$$

where $\sigma_{15} = 1082.9 \pm 4.0\,{\rm km\,s^{-1}}$, $\alpha = 0.3361 \pm 0.0026$, $h_{70}(z) = h_{70}\sqrt{\Omega_\Lambda + (1+z)^3 \Omega_M}$ for a flat cosmology and $\sigma_{\rm DM}$ is the one-dimensional velocity dispersion of the dark matter particles within r_{200c}, which is related to the velocity dispersion of galaxies by a so-called bias factor $b_v = S_{\rm BI}/\sigma_{\rm DM}$. As summarized by Evrard et al. (2008), the bias factor as currently estimated is $\langle b_v \rangle = 1.00 \pm 0.05$. For consistency with previous studies (e.g., Brodwin et al. 2010), we adopt a value $b_v = 1$, meaning that galaxies are unbiased tracers of the mass in a cluster.

The mass values drawn from Eq. 1 are shown in Table 3, and the given errors include uncertainties on the cluster redshift, the velocity dispersion, α and σ_{15}. The overall uncertainty in the mass is dominated by statistical errors which, in turn, are dominated by the error in the velocity dispersion. The systematics introduced by Eq. 1 contribute $< 10\%$ of the uncertainties listed in Table 3. The mass from Eq. 1 yields a lower value than the virial mass estimator, as Carlberg et al. (1997) also anticipated.

As indicated by Evrard et al. (2008), Eq. 1 holds for primary halos, i.e., clusters where a "main system" can be easily identified and substructure is only marginal. As noted in §4.2, a high fraction of the clusters have significant substructure, but none of them shows a clear bimodal distribution in velocity and we therefore assume that Eq. 1 is applicable to all the clusters in the sample.

The radius r_{200c} is also listed for each cluster in Table 3. These have been calculated using M_{200c} and assuming spherical clusters (i.e., $M_{200c} = 200\rho_c \times 4\pi r_{200c}^3/3$).

4.2. *Substructure*

It is becoming widely accepted that substructure is a common feature of galaxy clusters, and that its presence (or lack thereof) is related to the degree of relaxation and hence the validity of the hydrostatic equilibrium hypothesis (e.g., Battaglia et al. 2011, and references therein). While X-ray observations can reveal the presence of substructure in the plane of the sky, velocity information can reveal substructure in the radial direction. From X-ray observations over a wide range in masses at $z \lesssim 0.3$, Schuecker et al. (2001) find that $(52 \pm 7)\%$ of galaxy clusters present significant substructure. Girardi et al. (1997) find that out of 44 optically selected local ($z \leq 0.15$) clusters, 15 (38%) show significant signs of substructure based on their dynamics. Girardi et al. (1997) argue, on the other hand, that substructure found in clusters that show a *unimodal* velocity distribution (i.e., where the substructure is not of comparable size to the cluster itself) does not influence the velocity dispersion (hence mass) measurements.

In general, a non-negligible fraction of the galaxy clusters in a sample will have biased mass measurements due to substructure. These results highlight the need for a correct estimation of the degree to which galaxy clusters seem to be relaxed or in the process of merging.

One very basic test for substrucure involves the distribution of measured velocities. In fact, however, none of our velocity histograms shows clear evidence for a bi- or multimodal distribution and the velocity dispersions $S_{\rm BI}$ are consistent with Gaussian dispersions, in all cases, within 1σ. So, in the following, we employ three specific tests that take advantage of the 3-dimensional information provided by optical spectroscopy to assess the dynamical state of the clusters from a wide perspective. Table 4 summarizes the substructure analysis.

4.2.1. *1d: BCG Peculiar Velocity*

For a cluster that is relaxed, the peculiar velocity of the BCG should be close to zero (Quintana & Lawrie 1982; Oegerle & Hill 2001, but see Pimbblet et al. (2006) for a likely counter example). Oegerle & Hill (2001) find that the dispersion of BCG peculiar velocities is $\sim 160\,{\rm km\,s^{-1}}$ for a median $S_{\rm BI} \sim 800\,{\rm km\,s^{-1}}$. Using a sample of 452 clusters, Coziol et al. (2009) find that BCGs have a median peculiar velocity $0.32 S_{\rm BI}$ and that 41% of BCGs have velocities different from zero at the 2σ-level, but note that this number is comparable to the fraction of clusters that show signs of substructure. In summary, velocities consistent with zero are not necessarily expected. Dominant (D/cD) BCGs, however, are mostly found in the low peculiar velocity regime. Clusters are (provisionally) considered as disturbed if their BCG has a peculiar velocity different from zero at the 2σ-level where, following Coziol et al. (2009), the fractional uncertainties are given by

$$\Delta\left(v_{\rm pec}/S_{\rm BI}\right) = \frac{1}{S_{\rm BI}} \sqrt{\left(\Delta v_{\rm pec}\right)^2 + \left(\frac{v_{\rm pec}\Delta S_{\rm BI}}{S_{\rm BI}}\right)^2} \qquad (2)$$

where $\Delta v_{\rm pec} = \sqrt{S_{\rm BI}^2/N_{\rm gal} + (\Delta v_{\rm BCG})^2}$ is the error in the peculiar velocity, and $\Delta v_{\rm BCG}$ is twice the cross-correlation error estimated by RVSAO, which is a conservative correction

would be $\ll 1\%$, and still negligible over the statistical uncertainty in the velocity dispersion.

Table 3
Dynamical Properties of ACT 2008 Clusters

ACT Descriptor	$N_{\rm gal}$[a]	$z_{\rm BI}$	$S_{\rm BI}$ (km s^{-1})	r_{200c} (h_{70}^{-1} kpc)	M_{200c} ($10^{14}\,h_{70}^{-1}\,M_\odot$)
ACT-CL J0102–4915[b]	89	0.87008 ± 0.00010	1321 ± 106	1789 ± 140	16.3 ± 3.8
ACT-CL J0215–5212	55	0.48009 ± 0.00012	1025 ± 102	1736 ± 173	9.6 ± 2.8
ACT-CL J0232–5257	64	0.55595 ± 0.00009	884 ± 110	1438 ± 177	5.9 ± 2.2
ACT-CL J0235–5121	82	0.27768 ± 0.00006	1063 ± 101	2007 ± 190	11.9 ± 3.4
ACT-CL J0237–4939	65	0.33438 ± 0.00009	1280 ± 89	2339 ± 162	20.0 ± 4.2
ACT-CL J0304–4921	71	0.39219 ± 0.00008	1109 ± 89	1971 ± 155	12.7 ± 3.0
ACT-CL J0330–5227[c]	71	0.44173 ± 0.00009	1238 ± 98	2138 ± 166	17.1 ± 4.0
ACT-CL J0346–5438	88	0.52973 ± 0.00007	1075 ± 74	1770 ± 122	10.7 ± 2.2
ACT-CL J0438–5419[d]	65	0.42141 ± 0.00011	1324 ± 105	2310 ± 182	21.1 ± 5.0
ACT-CL J0509–5341[e]	76	0.46072 ± 0.00006	846 ± 111	1451 ± 189	5.5 ± 2.1
ACT-CL J0521–5104[f]	24	0.67549 ± 0.00032	1150 ± 163	1744 ± 245	12.1 ± 5.1
ACT-CL J0528–5259[g]	55	0.76780 ± 0.00010	928 ± 111	1337 ± 159	6.1 ± 2.2
ACT-CL J0546–5345[h]	48	1.06628 ± 0.00020	1082 ± 187	1319 ± 226	8.1 ± 4.2
ACT-CL J0559–5249[i]	31	0.60910 ± 0.00026	1219 ± 118	1916 ± 184	14.9 ± 4.3
ACT-CL J0616–5227	18	0.68380 ± 0.00044	1124 ± 165	1699 ± 244	11.2 ± 4.9
ACT-CL J0707–5522	58	0.29625 ± 0.00006	832 ± 82	1561 ± 156	5.7 ± 1.7

[a] Number of spectroscopically confirmed members, after applying the selection procedure of §3.2.
[b] "El Gordo" (Menanteau et al. 2011); SPT-CL J0102–4915 (Williamson et al. 2011).
[c] Abell 3128 (NE) (Werner et al. 2007).
[d] PLCK G262.7–40.9 (Planck Collaboration 2011a), SPT-CL J0438–5419 (Williamson et al. 2011).
[e] SPT-CL J0509–5341 (Staniszewski et al. 2009).
[f] SCSO J052113–510418 (Menanteau et al. 2010a), SPT-CL J0521–5104 (Vanderlinde et al. 2010).
[g] SPT-CL J0528–5259 (Staniszewski et al. 2009), SCSO J052803–525945 (Menanteau et al. 2010a).
[h] SPT-CL J0547–5345 (Staniszewski et al. 2009).
[i] SPT-CL J0559–5249 (Vanderlinde et al. 2010).

(Quintana et al. 2000).

Eight clusters meet this criterion, which will be coupled with similarly chosen criteria in the $2d$ and $3d$ analyses before selecting which clusters have significant evidence for substructure.

4.2.2. *2d: Projected BCG-SZE Offset*

Under the hypothesis of hydrostatic equilibrium, galaxies closely trace the total mass distribution in the cluster and thus the BCG is located at the peak of the gravitational potential. If the cluster is virialized, the gas should also follow the mass distribution. Deviation from this scenario may be quantified by an offset between the BCG (i.e., dark matter) and the SZE (i.e., gas) peak. This, of course, is sensitive to offsets projected in the sky, unlike the preceding and following tests.

ACT has a beam of $1\farcm4$ (FWHM) at 148 GHz (Hincks et al. 2010) and the uncertainties in the determination of the position of each cluster are of order $10''$-$15''$. We therefore list the projected offset in arcsec in Table 4; offsets $\lesssim 15''$ are within ACT's positional uncertainty and should therefore not be considered physical offsets. Column 6 of Table 4 lists the projected offset between the BCG and the SZE peak for each cluster relative to the characteristic scale of the cluster r_{200c}. Lin & Mohr (2004) find that $> 80\%$ of BCGs are offset from the peak gas emission by $\Delta r/r_{200c} < 0.2$. Moreover, Skibba et al. (2011) find that $\sim 40\%$ of BCGs do not sit at the minimum of the potential well in clusters.

We choose $\Delta r/r_{200c} \sim 0.20$ as the threshold between (tentatively classified) relaxed and disturbed clusters, based on the results of Lin & Mohr (2004). In this case, only three clusters—ACT-CL J0102–4915, ACT-CL J0509–5341, and ACT-CL J0528–5259—have values over the threshold. Given that the chance of line-of-sight (l.o.s.) substructure should be the same as that of substructure in the plane of the sky[6], this might be too stringent a limit. We note that the findings of Skibba et al. (2011) argue that this might not be a very reliable test for substructure, but we include it for completeness.

We note that these three clusters have offsets on the order of an arcminute, far beyond uncertainties in the ACT SZE centroids and therefore qualify as physical offsets.

4.2.3. *3d: DS Test*

By studying a large sample of statistical tests for substructure in galaxy clusters, Pinkney et al. (1996) have shown that the DS test (Dressler & Shectman 1988) is the most sensitive test when used individually. The test has the ability not only to detect the presence of substructure, but also to locate the latter in projected space (in the ideal cases of substructure not overlapping with the main system neither in velocity nor in projected space) and is based in the detection of localized subgroups of galaxies that deviate from the global distribution of velocities by use of the parameter $\Delta = \Sigma_i \delta_i$, where

$$\delta_i^2 = \frac{N_{\rm local}}{\sigma^2}\left[(\bar{v}_i - \bar{v})^2 + (\sigma_i - \sigma)^2\right]^2 \tag{3}$$

is computed for each cluster member, where $\bar{v}_i$ and σ_i are the mean and standard deviation of the velocity distribution of the $N_{\rm local}$ members closest to the ith member, and $\bar{v}$ and σ are the mean and standard deviation of the velocity distribution of all the cluster members. The significance level (s.l.) of the test is obtained by shuffling the velocities of each galaxy via a bootstrap resampling technique with 5000 iterations. Although the common use is that $N_{\rm local} = \sqrt{N_{\rm gal}}$, in this work Δ is calculated for $N_{\rm local}$ ranging from 5 to 12. The uncertainties in the s.l. are given by the second-maximum and second-minimum s.l. for each cluster when varying $N_{\rm local}$ (i.e., they correspond to $\sim 75\%$-level uncertainties), and the central value is given by the median. A large uncertainty (i.e., dependence on $N_{\rm local}$) might also be indicative of substructure, but we do not include this in the analysis.

---

[6] In fact, the latter should be approximately twice as large, given the number of dimensions covered by the plane of the sky and the l.o.s..

Table 4
Substructure in ACT 2008 Clusters

Cluster	z	$\lvert v_{\rm pec}\rvert$ [a] ($\rm km\,s^{-1}$)	$\lvert v_{\rm pec}\rvert / S_{\rm BI}$	Δr [b] (arcsec)	$\Delta r / r_{200c}$	s.l. (DS) [c]	Disturbed? [d]	
ACT-CL J0102–4915[e]	0.870	10 ± 169	0.01 ± 0.13	68	0.30	$0.48^{+0.13}_{-0.02}$	010	Yes
ACT-CL J0215–5212	0.480	1171 ± 153	1.14 ± 0.19	33	0.12	$0.02^{+0.00}_{-0.01}$	101	Yes
ACT-CL J0232–5257	0.556	37 ± 129	0.04 ± 0.14	35	0.15	$0.11^{+0.11}_{-0.05}$	000	No
ACT-CL J0235–5121	0.278	138 ± 137	0.13 ± 0.13	44	0.09	$0.04^{+0.01}_{-0.03}$	001	Yes
ACT-CL J0237–4939	0.334	261 ± 174	0.20 ± 0.14	78	0.16	< 0.01	001	Yes
ACT-CL J0304–4921	0.392	151 ± 157	0.14 ± 0.14	22	0.06	$0.04^{+0.09}_{-0.03}$	001	No
ACT-CL J0330–5227	0.442	424 ± 167	0.34 ± 0.14	44	0.12	$0.21^{+0.27}_{-0.02}$	100	No
ACT-CL J0346–5438	0.530	263 ± 125	0.24 ± 0.12	16	0.06	$0.23^{+0.05}_{-0.07}$	100	No
ACT-CL J0438–5419	0.421	392 ± 172	0.30 ± 0.13	10	0.02	$0.03^{+0.01}_{-0.02}$	101	Yes
ACT-CL J0509–5341	0.461	361 ± 134	0.42 ± 0.17	114	0.46	$0.08^{+0.04}_{-0.03}$	110	Yes
ACT-CL J0521–5104[f]	0.676	440 ± 292	0.37 ± 0.25	37	0.15	—	00-	No?
ACT-CL J0528–5259	0.768	144 ± 177	0.16 ± 0.19	50	0.28	$0.30^{+0.07}_{-0.02}$	010	No
ACT-CL J0546–5345	1.066	541 ± 163	0.50 ± 0.17	20	0.13	$0.02^{+0.04}_{-0.02}$	101	Yes
ACT-CL J0559–5249	0.609	233 ± 241	0.19 ± 0.20	9	0.03	$0.13^{+0.13}_{-0.06}$	000	No
ACT-CL J0616–5227[f]	0.684	685 ± 268	0.61 ± 0.25	29	0.12	—	10-	Yes?
ACT-CL J0707–5522	0.296	402 ± 140	0.48 ± 0.18	19	0.05	$0.34^{+0.04}_{-0.15}$	100	No

Note. — Redshifts are listed for reference.

[a] Peculiar velocity of the BCG in the cluster rest-frame (see §4.2.1). The uncertainties consider the error on the BCG redshift as twice that given by RVSAO.

[b] Offset between the BCG and the SZ peak as found in the Y_{200c} analysis (see §§2.1,4.2.2 for details).

[c] Significance level of the DS test. Uncertainties are computed at the 75% level (see §4.2.3 for details).

[d] Each ordered number represents one of the tests listed in the table: "1" means the tests shows evidence for substructure and "0" means it does not.

[e] This cluster is classified as "disturbed" based on the results of Menanteau et al. (2011). See text for details.

[f] There are too few members observed for the DS test to be reliable. The classification is left as a tentative one, and these clusters are excluded from the analysis of §5.3 (see 4.2.4).

As shown by Pinkney et al. (1996), the false positive rate for the DS test is $< 1\%$, $< 4\%$ and 9% for a s.l. of 1%, 5% and 10% respectively, for member samples as large as ours. The threshold for substructure detection is set therefore at 5% s.l. within uncertainties where, given the size of our sample, we expect no false detections.

4.2.4. *Substructure Results*

Clusters have been identified as merging systems if they meet at least two of the three conditions explained above, or if they have a s.l. of the DS test *strictly* below 5% within uncertainties. Although the second of the three conditions depends on the projected spatial distribution, it is clear that this analysis is biased towards l.o.s. substructure.

ACT-CL J0102–4915 ("El Gordo") is a special case, as it does not show evidence for merging from the dynamical information alone. However, both the spatial galaxy distribution and X-ray surface brightness distribution reveal that this is a very complex system where two massive clusters are interacting close to the plane of the sky (Menanteau et al. 2011).

On the other hand, ACT-CL J0616–5227 is tentatively considered as a merging cluster given the high peculiar velocity of the BCG, but the DS test was not performed for this cluster given the low number of members. The latter note also applies to ACT-CL J0521–5104, although this cluster is tentatively considered relaxed. These two clusters have been excluded from the analysis of §5.3.

The last column of Table 4 states whether a cluster is considered to be relaxed ("No") or disturbed ("Yes") while the previous column lists whether each cluster shows ("1") or does not show ("0") signs of substructure in each of the tests, as defined above. Combining the three criteria used, 7 out of 14 clusters show signs of merger activity (or 8 of 16, if we include ACT-CL J0616–5227 and ACT-CL J0521–5104). This number is consistent with previous optical and X-ray studies of local clusters (e.g., Girardi et al. 1997; Schuecker et al. 2001) and is also consistent with the X-ray follow-up of SPT SZE-detected clusters by Andersson et al. (2011). They find that 9 out of 15 SZE-selected clusters show signs of substructure based purely on X-ray morphology.

4.3. *The Influence of Emission-Line Galaxies*

Clusters of galaxies are mostly populated by passive galaxies. Late-type galaxies are preferentially found in the outskirts of clusters and associated with infalling groups. They therefore tend to show a different velocity distribution (Biviano & Katgert 2004). Girardi et al. (1996) find that 29% (53%) out of a sample of 17 nearby clusters show differences in the velocity dispersion and 24% (47%) in the mean velocity, at the 2σ (1σ) level. Simulations also show that, where blue galaxies are found (i.e., outside the core), they tend to have a higher velocity dispersion than red galaxies (Springel et al. 2001b). The way blue galaxies are distributed in the cluster (both in space and in velocity) depends, however, on the history of each cluster (Biviano & Katgert 2004). The issue is complex; for example Aguerri & Sánchez-Janssen (2010) find no difference in the fraction of blue galaxies between relaxed and disturbed clusters.

Although our target selection procedure should not be strongly biased against emission-line galaxies, the observa-

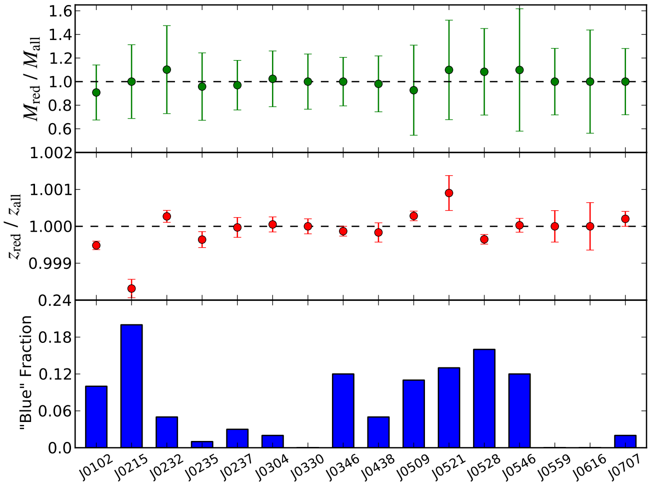

Figure 3. The top two panels show, for each cluster indicated on the horizontal axis, the ratios of dynamical masses *(top)* and cluster redshifts *(middle)* when only the absorption-line ("red") galaxies or all galaxies are used for the analysis. Error bars are given by $\Delta M_{\rm all}/M_{\rm all}$ and $\Delta z_{\rm all}/z_{\rm all}$, respectively. The dashed line in each panel marks a ratio of unity. The *bottom* panel shows the observed fraction of galaxies with emission lines ("blue"). Cluster names have been shortened for clarity. (See the text for details.)

tions have not been designed to study this effect and the spectroscopic samples have emission-line fractions of $\lesssim$ 10% in most cases. This number does not necessarily reflect the actual fraction in the clusters and could be taken as a lower limit for it. In spite of all this, we briefly study the effect that blue[7] galaxies might have on the results.

Fig. 3 shows, in the top and middle panels respectively, the variation of the mass measurement and the cluster redshift when blue (i.e., emission-line) galaxies are, and are not, included. The null hypothesis (i.e., no bias) corresponds to $M_{\rm red}/M_{\rm all} = 1$. Within uncertainties (given by $\Delta M_{\rm all}/M_{\rm all}$), dynamical masses do not change when including emission-line galaxies. Some cluster redshifts, however, change significantly. Four clusters have different redshifts at the 2σ-level. The two most extreme cases are ACT-CL J0215–5212, for which the redshifts calculated including, or not, blue galaxies, are different at the 6.5σ-level, and ACT-CL J0102–4915, at the 4.5σ-level. Note that for the red-only analysis, the blue galaxies are removed before the selection process (i.e., $N_{\rm red}$ does not necessarily equal $N_{\rm gal} - N_{\rm blue}$).

The redshifts, velocity dispersions and corresponding masses in Table 3 have been calculated using all galaxies, since blue galaxies do not bias our mass measurements. This, in turn, is consistent with the findings of Aguerri & Sánchez-Janssen (2010).

5. SZE-MASS SCALING RELATIONS

Both Vanderlinde et al. (2010) and Sehgal et al. (2011) have shown that, given an accurate calibration of the SZE-Mass scaling relation, the inclusion of the ACT or SPT cluster samples can lead to significant improvements in cosmological parameter uncertainties, particularly w and σ_8, over WMAP-7–only constraints. These results have recently been confirmed by Benson et al. (2011) using X-ray observations. However, without a precise SZE-Mass scaling relation, these cluster samples do not provide significant improvements in constraining cosmological parameters. Determining a precise and accurate scaling relation characterizing the mass of a cluster in terms of its SZE signal is the main goal of this study.

Observations have shown that the SZE signal and mass of a cluster can be related by a power-law (Benson et al. 2004; Bonamente et al. 2008; Melin et al. 2011). While most simulations seem to confirm this (da Silva et al. 2004; Motl et al. 2005; Nagai 2006), others suggest that certain effects (e.g., AGN feedback) can cause deviations from a single power-law dependence (Battaglia et al. 2011). In this work, we restrict ourselves to a power-law relation between dynamical mass (see §4 and Table 3) and each SZE estimator measured from the ACT data (see §2.1.2 and Table 1) of this form:

$$M_{200c} = 10^A \left[y_{0!5} E(z)^{-2}\right]^B h_{70}^{-1} M_\odot \tag{4a}$$

$$M_{200c} = 10^A \left[y_0 E(z)^{-2}\right]^B h_{70}^{-1} M_\odot \tag{4b}$$

$$M_{200c} = 10^A \left[Y_{200c} D_A(z)^2 E(z)^{-2/3}\right]^B h_{70}^{-1} M_\odot \tag{4c}$$

where $D_A(z)$ is the angular diameter distance in Mpc, M_{200c} is in units of $h_{70}^{-1} M_\odot$ and $E(z) = [\Omega_M(1+z)^3 + \Omega_\Lambda]^{1/2}$. We refer to B as the (logarithmic) slope of the scaling relations. The self-similar predictions are 1, 1, and 0.6 for the $y_{0.5'}$, y_0 and Y_{200c} scalings, respectively (e.g., Bonamente et al. 2008; Marriage et al. 2011a; Sehgal et al. 2011). We note that these are convenient forms of parameterizing the scaling relations if one wants to predict the mass of a cluster using SZE observations.

Before we proceed to estimate scaling laws we consider the selection biases, specifically Malmquist and Eddington, that can affect our study when fitting the scaling relations (see Mantz et al. 2010a, for a pedagogical description). The Eddington bias results from the asymmetry of the steep underlying mass function (e.g., Jenkins et al. 2001; Tinker et al. 2008) which introduces a shift in mass due to the statistical fluctuations of the measurement of the mass proxy in the observable-mass relation. The dynamical-mass scaling relations used here (Evrard et al. 2008) were calculated from cosmological simulations that inherently take into account the proper asymmetric mass function and therefore are not subject to Eddington bias. Our sample, however, has been selected based on SZE signal, which makes it subject to Malmquist bias with the largest biases experienced by clusters near the detection threshold of the survey. In the following section we describe our methodology to correct for this bias.

5.1. *Malmquist Bias Correction*

The Malmquist bias is produced by the intrinsic scatter in the observable: clusters with mean SZE fluxes at the detection limit whose signals scatter up will make it into the sample, while those that scatter down will not. We use the simulations of Sehgal et al. (2010) to investigate this effect in our sample, by measuring y_0 in the simulated clusters (Hasselfield et al. 2012, in prep.) in the exact same way as for the observed clusters and subsequently applying a cut ($y_0 T_{\rm CMB} > 150 \mu K$) to the simulated data that reflects approximately the detection threshold of the observed cluster sample. This procedure mimics the observational situation with the exception that it assumes a constant noise level throughout the survey. The ACT sample is defined in terms of a S/N limit, although the

---

[7] Although the classification is done purely based on the spectral features of each galaxy (with- or without emission lines), we sometimes speak of blue and red, instead of emission- and absorption-line galaxies respectively, for convenience.

Table 5
Best-fit parameters of scaling relations

Relation	$B_{\rm SS}$[a]	A	B	σ_{MY}
		Best-fit		
$y_{0'.5}^{\rm corr} - M_{200c}$	1	20.0 ± 1.9	1.16 ± 0.27	0.16 ± 0.03
$y_{0}^{\rm corr} - M_{200c}$	1	18.2 ± 0.7	0.74 ± 0.11	0.12 ± 0.02
$Y_{200c}^{\rm corr} - M_{200c}$	0.6	17.0 ± 1.6	0.56 ± 0.11	0.11 ± 0.02

[a] Expected logarithmic slope from self-similar evolution.

noise level is approximately constant except near the edges of the map (Marriage et al. 2011a,b). Within our sample, there is potentially only one cluster (ACT-CL J0707–5522) whose Malmquist correction is not accurately described by this procedure because it sits in a high-noise region in the maps. If this cluster is removed from the sample, the change in the Malmquist-corrected scaling laws is negligible. In practice, clusters within a mass range from M to $M + \Delta M$ are extracted from the simulations and the average y_0 value of the extracted subsample is determined both with and without a detection threshold. The ratio of y_0 values represents a statistical estimate of the Malmquist bias factor for clusters within this mass range. The procedure is repeated for different mass ranges that span the ACT cluster sample. At the low mass end of the cluster sample the bias correction factor is ~ 0.8, while for clusters with $M_{200c} > 9 \times 10^{14} M_\odot$ the correction factor is close to unity. A continuous smooth curve is fitted to the bias correction factors as a function of mass and applied individually to each cluster's individual measured y values. To distinguish the bias-corrected values hereafter, we label them with a superscript "corr". We apply the same bias correction factors to each of the different SZE estimators. This is a reasonable approach since the latter are all based on matched filters with kernels of similar scales.

5.2. *Best-fit Scaling Relations*

We use the Bivariate Correlated Errors and intrinsic Scatter (BCES) bisector algorithm for linear regression (Akritas & Bershady 1996), which takes into account measurement errors in both axes and intrinsic scatter, to find the best-fit slopes and normalizations of the power-law scaling relations given by Eqs. 4. The results are shown in Fig. 4, where the solid lines represent the best-fit power-laws and the shaded regions are the 1σ uncertainties. Table 5 lists the best-fit parameters, where the last column lists the log-normal intrinsic scatter orthogonal to the best-fit line, as introduced by Pratt et al. (2009). Uncertainties in the intrinsic scatter are computed following Planck Collaboration (2011b). Different symbols identify the dynamical state of each cluster (see §5.3).

All three SZE estimators correlate with dynamical mass with Pearson's r-values of 0.63, 0.75 and 0.67 for $y_{0'.5}^{\rm corr}$, $y_0^{\rm corr}$ and $Y_{200c}^{\rm corr}$, respectively. The fractional errors on the slopes are similar, ranging from 15% for $y_0^{\rm corr} - M_{200c}$ to 25% for $y_{0'.5}^{\rm corr} - M_{200c}$, while σ_{MY} ranges from 11% to 16% depending on the SZE estimator. These values are consistent with those found in simulations (which have some dependence on the input cluster physics) and are of order 10%-15% for large-aperture integrations such as Y_{200c} (Nagai 2006; Yang et al. 2010; Battaglia et al. 2011). We find that the intrinsic scatter of the $y_0^{\rm corr} - M_{200c}$ relation is low and similar to that of the $Y_{200c}^{\rm corr} - M_{200c}$ scaling law. While numerical simulations predict a higher dependence on gas physics and projection effects for central estimates (e.g., Motl et al. 2005; Shaw et al.

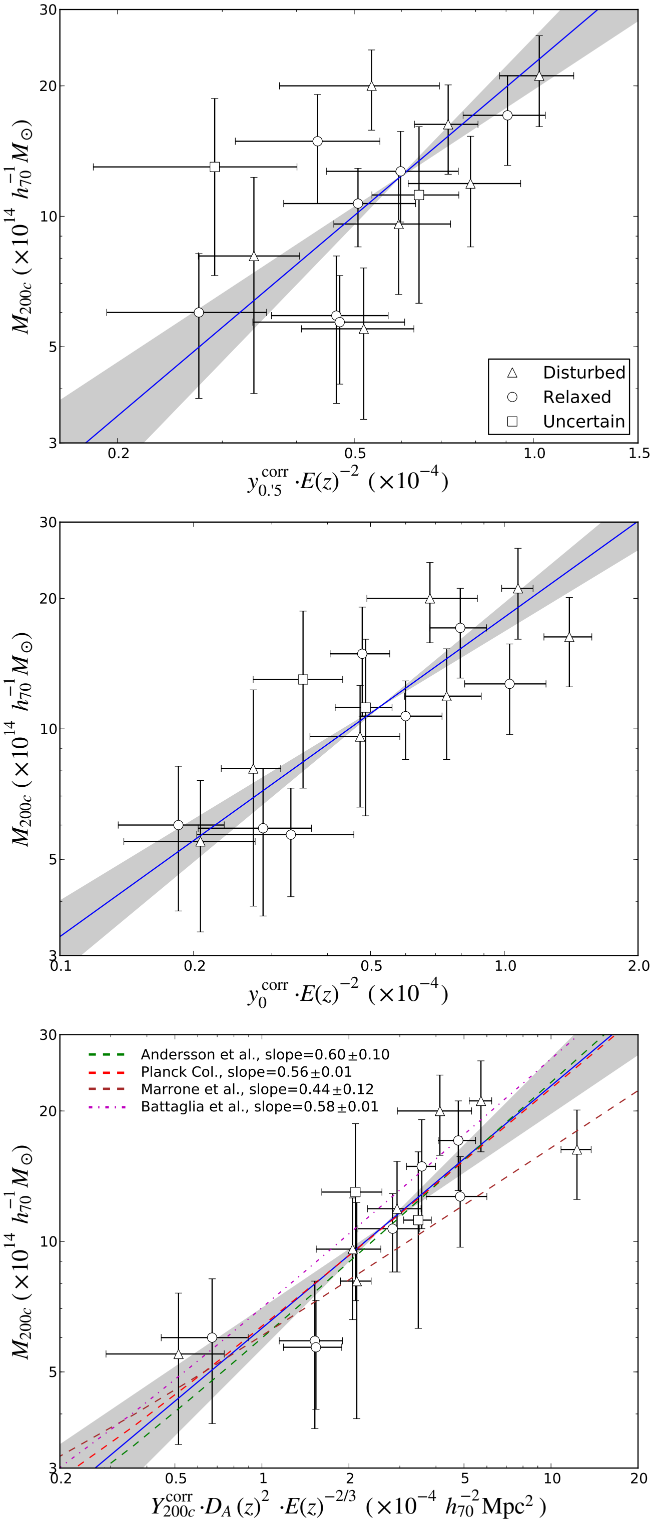

Figure 4. Scaling relations between SZE estimators and dynamical mass for $y_{0'.5}$ from Sehgal et al. (2011) with ACT 2008 data *(top)*, the central SZE amplitude y_0 *(middle)*, and Y_{200c}, the Compton y-parameter integrated out to r_{200c} *(bottom)*, the latter two including three-season ACT data. All estimators have been scaled as indicated in the axis labels (see Eqs. 4) and data points have been corrected for Malmquist bias as detailed in the text. Solid blue lines show the best-fit power laws, with the 1σ uncertainties marked by the shaded regions (see Table 5). Different symbols identify whether each cluster is disturbed (triangles), relaxed (circles), or not classified (squares). Previous estimates of the Y_{200c}–M_{200c} scaling relation are shown in the bottom panel with dashed and dot-dashed lines (see text for details).

Table 6
Best-fit parameters of scaling relations for selected subsamples

Relation	Sample	A	B	σ_{MY}
$y^{\rm corr}_{0'.5} - M_{200c}$	Disturbed	20.7 ± 5.1	1.34 ± 0.76	0.18 ± 0.05
	Relaxed	20.5 ± 6.6	1.29 ± 0.98	0.17 ± 0.05
$y^{\rm corr}_{0} - M_{200c}$	Disturbed	18.0 ± 1.3	0.69 ± 0.19	0.13 ± 0.04
	Relaxed	18.4 ± 2.0	0.79 ± 0.27	0.13 ± 0.04
$Y^{\rm corr}_{200c} - M_{200c}$	Disturbed	16.8 ± 2.3	0.50 ± 0.16	0.14 ± 0.04
	Relaxed	17.3 ± 2.4	0.65 ± 0.17	0.09 ± 0.03

Note. — There are 7 merging and 7 relaxed clusters. See text for details.

2008), comparison of the former with simulations should be done with care since, as stated in §2.1.2, y_0 here is not necessarily the projected central pressure of the cluster as is often defined in simulations, but the normalization of the A10 profile in the optimally filtered maps. For this reason, comparison with self-similarity is also not straightforward for $y_0^{\rm corr} - M_{200c}$.

5.3. *Scaling Relations for Relaxed and Disturbed Clusters*

Table 6 lists the best-fit scaling relations when separating the sample into relaxed and disturbed clusters according to Table 4 (see §4.2). The effect of disturbed clusters, if any, is similar for all SZE estimators and is apparent as a slight, but not significant, change in slope and an increase of σ_{MY}. While errors on samples of this size are very large, we find that $Y^{\rm corr}_{200c} - M_{200c}$ has the largest decrease in scatter when including only relaxed clusters, and the largest boost for disturbed clusters. Also, and contrary to expectations, the change in slope is largest for the $Y^{\rm corr}_{200c} - M_{200c}$ scaling relation.

Of the 7 merging clusters, 5 are at low redshift ($z < 0.5$) and of the 7 relaxed clusters, 4 are at high redshift ($z > 0.5$). We have explored redshift-induced biases in the scaling relations and find that they are dependent on the fraction of merging clusters in each sample. In this way, the high-z sample is consistent with the relaxed sample and the low-z sample is consistent with the merging sample.

As explained in §4.2, neither ACT-CL J0521–5104 nor ACT-CL J0616–5227 have been considered in the present analysis. Including these clusters in either sample does not change the best-fit parameters and only changes the intrinsic scatter by $\lesssim 0.05$.

5.4. *Previous Results*

Rines et al. (2010) were the first to present a comparison of SZE fluxes and masses derived from dynamical information, but their sample selection did not allow for the estimation of a scaling relation. Here, we review some SZE-Mass scaling relations derived from other observations or mass proxies. While we note that many authors have presented scaling relations in different forms and using a variety of mass proxies, here we compare to those that have done so in the same form as is done here (i.e., correcting by intrinsic evolution). When appropriate, cylindrical Y_{200c} measurements have been converted to spherical equivalents applying the correction for the A10 profile.

When comparing to other results we have converted to values calculated within r_{200c} by assuming that M scales as $M \propto Y^{\alpha}$ using the respective profiles found by each study. The normalization was estimated as the ratio of the NFW profile used for the mass and the GNFW profile used for Y_{200c}.

The bottom panel of Fig. 4 shows these scaling relations; those where masses were estimated from X-ray observations (Andersson et al. 2011; Planck Collaboration 2011b) and weak-lensing measurements (Marrone et al. 2011) are shown with dashed lines, and the dash-dotted line shows the results from hydrodynamical simulations by Battaglia et al. (2011).

All the scaling relations are in good agreement with that presented here. The scaling derived by Marrone et al. (2011) has a shallower, but consistent, slope than all the other scaling relations. The scaling relation derived in this work is in excellent agreement with those by Andersson et al. (2011) and Planck Collaboration (2011b), both derived with X-ray mass estimates of SZE-selected clusters.

6. DISCUSSION

6.1. *Individual Clusters*

In this section we list clusters with notable features, including comparison of dynamical masses presented here with previous estimates, where available.[8] The respective original or alternative names can be found in Table 3. With respect to notes on optical features of these clusters, the reader is referred to Figs. 4-10 of Menanteau et al. (2010b), as appropriate.

6.1.1. *ACT-CL J0102–4915 "El Gordo"*

Located at $z = 0.870$, this cluster has the largest SZE signal (it is the rightmost data point in the top and bottom panels of Fig. 4) and is one of the most massive clusters of the sample according to its dynamics. This cluster looks elongated in the optical (in fact, it is double-peaked in the galaxy distribution; Menanteau et al. 2011), but there are no clear signs of line-of-sight substructure from the dynamical information. In Menanteau et al. (2011), we show that if the cluster is divided into two subclusters in the process of merging (as suggested by the optical data), they have a mass ratio of order 2:1, with a total summed dynamical mass of $M_{200c} = (24 \pm 7) \times 10^{14}\, h_{70}^{-1} M_{\odot}$, making this a huge merger between two already massive clusters.

Menanteau et al. (2010b) used a multi-wavelength data-set combining X-rays, SZE and the information provided in this work to estimate the cluster mass using several mass proxies which are in statistical agreement, with a combined mass estimate of $M_{200a} = 21.6 \pm 3.2 \times 10^{14}\, h_{70}^{-1} M_{\odot}$. The statistical error for the combined mass is likely an underestimate given the complex nature of this massive merging cluster (see Menanteau et al. 2011, for a fuller discussion of the mass measurements in "El Gordo")

6.1.2. *ACT-CL J0215–5212*

As shown in Table 4, this cluster appears to have substructure with a high significance as given by the DS test. More noteworthy, however, is the peculiar velocity of the BCG, $v_{\rm pec} = 1171 \pm 153\,{\rm km\,s^{-1}}$, different from zero at $> 7.5\sigma$. This is the only cluster in our sample in which the velocity of the BCG is comparable to the velocity dispersion of the cluster, and the cluster where the emission-line galaxies are most different from the whole population. ACT–CL J0215-5212 has a second galaxy $\sim 23''$ away (corresponding to a projected distance of $140\, h_{70}^{-1}$ kpc at $z = 0.480$) which is only 0.27 mag fainter and has a peculiar velocity of roughly $-660\,\mathrm{km\,s^{-1}}$, and at least three more galaxies within 0.55 mag of the BCG (which is the brightest of all by definition, but is also the one nearest to the optical center of the cluster), all of which have comparable ($\sim 1000\,\mathrm{km\,s^{-1}}$) peculiar velocities. On the other hand, this cluster does not significantly depart from any of the scaling relations of Fig. 4, showing the complexity of substructure analyses. It also has the highest fraction of emission-line galaxies.

---

[8] We quote the original mass estimates, given as M_{500c}—also with respect to the *critical* density of the Universe— and assume a typical conversion factor $M_{200c} \approx 1.6 M_{500c}$ (Duffy et al. 2008) when comparing with our results. In the particular case of "El Gordo", masses are originally given as M_{200a}, the masses within a radius containing 200 times the *average* density of the universe. For this cluster, the conversion is $M_{200c} \approx 0.86 M_{200a}$.

6.1.3. *ACT-CL J0237–4939*

Similar to the previous case, this cluster has 3 bright galaxies within $2'$ of the BCG, which are within 1 mag of the BCG. In particular, the second-brightest galaxy is $65''$ ($310\,h_{70}^{-1}$ kpc) away from the BCG, is 0.49 mag fainter and has a peculiar velocity with respect to the cluster of $\sim 1850\,\mathrm{km\,s^{-1}}$. All this argues in favor of the classification of this cluster as a disturbed system.

6.1.4. *ACT-CL J0330–5227*

As mentioned in §2.1.1, this cluster was discovered by Werner et al. (2007) behind Abell 3128 ($z = 0.06$) using *XMM-Newton* X-ray observations. The SZE measurement is clearly associated with the background structure while the less massive, foreground cluster has no significant SZE emission (Hincks et al. 2010). The dynamical mass estimated here is significantly higher than that derived by Werner et al. (2007), of $M_{500c} = 3.4 \times 10^{14}\,h_{70}^{-1}\,M_\odot$. They do caution, however, that their estimate is uncertain, as it is based on an isothermal beta-model for the cluster. Being located only $12'$ away from Abell 3128 at $z = 0.06$ on the sky, this cluster is a clear illustration of the mass selection of SZE surveys, approximately independent of redshift.

6.1.5. *ACT-CL J0438–5419*

ACT-CL J0438–5419 is the only new ACT cluster also reported by the Planck satellite (PLCKESZ G262.7–40.9, Planck Collaboration 2011a). It has been followed-up with *XMM-Newton*, with which Planck Collaboration (2011d) estimated a mass $M_{500c} = (6.9 \pm 0.7) \times 10^{14}\,h_{70}^{-1}\,M_\odot$ using a Y_X–M scaling. This value is 1.6σ lower than our dynamical estimate; in fact, this cluster is one of the most massive ones in our sample.

This cluster is also reported in Williamson et al. (2011). They estimate a simulation-based SZE-estimated mass $M_{500c} = (8.2 \pm 2.5) \times 10^{14}\,h_{70}^{-1}\,M_\odot$, consistent with both our mass estimates within 1σ. The *XMM-Newton* value is significantly lower than the other estimates, perhaps a result of the disturbed state of the cluster, as we propose here.

6.1.6. *ACT-CL J0509–5341*

This was one of the first clusters discovered by SPT (Staniszewski et al. 2009) and the first mass measurements were reported by Menanteau & Hughes (2009). Vanderlinde et al. (2010) reported a simulation–based SZE estimate of the mass of $M_{500c} = (4.3 \pm 1.1) \times 10^{14}\,h_{70}^{-1}\,M_\odot$ and Andersson et al. (2011) estimated an X-ray Y_X–derived mass from $M_{500c} = (5.4 \pm 0.6) \times 10^{14}\,h_{70}^{-1}\,M_\odot$. All previous values are in agreement with our estimate. Consistent with our substructure analysis, Andersson et al. (2011) found that this cluster is a disturbed system based solely on X-ray morphology.

6.1.7. *ACT-CL J0521–5104*

This cluster is not reported in Marriage et al. (2011a), because it was not a S/N>3 detection in the initial analysis. However, more recent analyses including data from 3 years of observations show that this cluster is now detected at 4.5σ, and it is therefore included in this study. Vanderlinde et al. (2010) report an SZE–estimated mass of $M_{500c} = (2.97 \pm 0.89) \times 10^{14} h_{70}^{-1} M_\odot$, significantly lower than the dynamical mass reported here.

6.1.8. *ACT-CL J0528–5259*

This cluster was also reported by Staniszewski et al. (2009) and characterized optically by Menanteau & Hughes (2009) Its SZE–estimated mass is $M_{500c} = (2.9 \pm 0.9) \times 10^{14}\,h_{70}^{-1}\,M_\odot$ (Williamson et al. 2011) and its X-ray–estimated mass is $M_{500c} = (3.0 \pm 0.9) \times 10^{14}\,h_{70}^{-1}\,M_\odot$ (Andersson et al. 2011). These values are consistent with our dynamical estimate. Also consistent with the present finding, Andersson et al. (2011) found that the X-ray morphology shows this cluster to be relaxed.

6.1.9. *ACT-CL J0546–5345*

This is the highest-redshift cluster of the sample, at $z = 1.066$. Brodwin et al. (2010) first presented a spectroscopic study of this cluster based on 18 cluster members, which have been included in this study, including the three emission-line galaxies not used for their mass measurement. We included Brodwin et al. (2010)'s galaxies in our spectroscopic catalog and applied the cluster membership algorithm (§3.2) which resulted in 48 members in total. Our mass estimate, calculated now with three times as many galaxies, is consistent both with their dynamical estimate and their best estimate, combining X-ray, SZE and dynamical information, which corresponds to $M_{200c} = (7.9 \pm 0.9) \times 10^{14}\,h_{70}^{-1}\,M_\odot$.

6.1.10. *ACT-CL J0559–5249*

This cluster was also detected by SPT and reported in Vanderlinde et al. (2010). They report a simulation–based SZE–derived mass $M_{500c} = (5.3 \pm 1.2) \times 10^{14}\,h_{70}^{-1} M_\odot$, while Andersson et al. (2011) estimate an X-ray Y_X–derived mass of $M_{500c} = (6.4 \pm 0.5) \times 10^{14}\,h_{70}^{-1} M_\odot$. Both these estimates are consistent with each other, and combined are consistent with the lower limit of our dynamical estimate. The ACT SZE signal is consistent with the dynamical mass (cf. Fig. 4). Using X-ray data, Andersson et al. (2011) suggest that this cluster is in the process of merging but our substructure analysis finds no evidence for substructure. These two results are not necessarily in contradiction since X-ray morphology and dynamical information are sensitive to substructure with different orientations.

6.1.11. *ACT-CL J0616–5227*

The optical imaging of this cluster by Menanteau et al. (2010b) was sufficient to provide confirmation but shallower than required to secure an adequate galaxy catalog for spectroscopic targeting. Out of 73 spectra obtained, only 18 are cluster members. Another 6 are foreground/background galaxies. The remaining are all late-type (mostly M) stars, which have similar colors to the cluster members. Both the SZ signal and the X-rays argue in favor of this being a massive cluster, supporting the dynamical estimate. This cluster readily shows the power of the SZE to reveal high-redshift clusters over optical selection techniques.

6.2. *The SCS clusters*

Of the 19 clusters observed during this program (see Table 2), only the 16 listed in Table 3 were detected by ACT. The other 3 clusters are listed in Table 7. These 3 clusters (hereafter "the SCS clusters") were discovered optically in the SCS and were included in the spectroscopic program because of their high optical richness (Menanteau et al. 2010a), along with ACT-CL J0521−5104. While their redshifts are consistent with the ACT sample, all three SCS clusters are in agreement with having dynamical masses low enough to be below the detection threshold of ACT, and provide additional evidence that the present sample is approximately mass-limited in nature.

7. CONCLUSIONS

We have conducted a large spectroscopic follow-up program of clusters of galaxies discovered via the Sunyaev-Zel'dovich effect by ACT in its southern sky survey (Marriage et al. 2011a; Menanteau et al. 2010b). We used 89 hours of multi-object spectroscopic observations divided between FORS2 at VLT and GMOS at Gemini-South. With a few (3-4) hours of observation per cluster, we have been able to confirm an average 65 members per cluster, which allowed us to: 1) obtain robust redshifts for each cluster; 2) measure velocity dispersions with errors $\lesssim 10\%$, which translates to uncertainties of $< 30\%$ in mass estimates; and 3) determine the dynamical state of the clusters.

The cluster sample spans a redshift range $0.28 < z < 1.07$, with a median redshift $z = 0.50$. Careful examination of possible substructure shows that $\sim 50\%$ of the clusters in the ACT sample contain significant substructure, consistent with the X-ray study of SPT SZE-selected clusters (Andersson et al. 2011) and with optically– and X-ray–selected local clusters. We find that the presence of emission-line galaxies within clusters, which could be associated with infalling groups, does not significantly modify the mass estimates. For this reason, emission-line galaxies have been included as members in the final samples.

Dynamical masses have been estimated from the radial velocity dispersions using the Evrard et al. (2008) simulation-based $\sigma - M_{200c}$ scaling relation. These clusters have masses $5 \lesssim M_{200c} \lesssim 22$ in units of $10^{14}\,h_{70}^{-1}\,M_{\odot}$, with a median mass $\sim 11 \times 10^{14}\,h_{70}^{-1}\,M_{\odot}$ in agreement with the mass distribution of the ACT sample as simulated by Marriage et al. (2011a) and estimated by Menanteau et al. (2010b). These clusters rank therefore among the most massive clusters in the Universe.

The scaling relation between dynamical mass and SZE signal has been studied using three estimators of the SZE: the single-season Compton signal within a $0'.5$-width pixel, $y_{0'.5}$, the central SZE amplitude, y_0, and the Compton signal integrated within r_{200c}, Y_{200c}. In order to derive unbiased scaling relations a simulation-based Malmquist bias correction has been applied to the data, and the scaling relations include intrinsic evolution with redshift.

These scaling relations are summarized in Table 5 and represent the main result of this work. The intrinsic scatter in these relations is consistent with that predicted by simulations (e.g., Motl et al. 2005; Reid & Spergel 2006). We find that Y_{200c} is our most robust mass proxy, with a log-normal intrinsic scatter of $11 \pm 2\%$. In all three SZE estimators, disturbed clusters do not bias the scaling relations but might slightly boost the intrinsic scatter (a $\sim$ 2-5% effect), which is lowest ($9 \pm 3\%$) for the $Y_{200c}^{\rm corr}$–M_{200c} relation for relaxed clusters. All this is in broad agreement with numerical simulations (e.g., Battaglia et al. 2011), and in excellent agreement with scaling relations derived with SPT and Planck data (Andersson et al. 2011; Planck Collaboration 2011b). We find that the intrinsic scatter of the $y_0^{\rm corr}$–M_{200c} relation is similar to that of $Y_{200c}^{\rm corr}$–M_{200c}.

In summary, the first sample of ACT spectroscopically followed-up SZE-selected clusters has provided results that agree with the expectations for the first-generation of SZE surveys. Scaling relations derived from this sample also agree with the expectations, increasing our confidence in the utility of the SZE for detecting and characterizing massive clusters at all redshifts and thus constraining cosmological parameters.

This work was supported by the U.S. National Science Foundation through awards AST-0408698 for the ACT project, and PHY-0355328, AST-0707731 and PIRE-0507768 (award number OISE-0530095). The PIRE program made possible exchanges between Chile, South Africa, Spain and the US that enabled this research program. Funding was also provided by Princeton University and the University of Pennsylvania. Computations were performed on the GPC supercomputer at the SciNet HPC Consortium. SciNet is funded by: the Canada Foundation for Innovation under the auspices of Compute Canada; the Government of Ontario; Ontario Research Fund – Research Excellence; and the University of Toronto. This research is partially funded by "Centro de Astrofísica FONDAP" 15010003, Centro BASAL-CATA, by FONDECYT under project 1085286 and by ALMA under projects 31090002 and 31100003.

REFERENCES

Abazajian, K. N., et al., 2009, ApJ, 182, 543
Aguerri, J. A. L., & Sánchez-Janssen, R., 2010, A&A, 521, A28
Akritas, M. G., & Bershady, M. A., 1996, ApJ, 470, 706
Andersson, K., et al., 2011, ApJ, 738, 48
Appenzeller, I., et al., 1998, The Messenger, 94, 1
Ashfordi, N., 2008, ApJ, 686, 201
Arnaud, M., Pratt, G. W., Piffaretti, R., Böhringer, H., Croston, J. H., & Pointecouteau, E., 2010, A&A, 517, A92
Bahcall, N. A., & Fan, X., 1998, ApJ, 504, 1
Balogh, M. L., Morris, S. L., Yee, H. K. C., Carlberg, R. C., & Ellingson, E., 1999, ApJ, 527, 54
Battaglia, N., Bond, J. R., Pfrommer, C., & Sievers, J. L., 2011, arXiv:1109.3709
Battye, R. A., & Weller, J., 2003, Phys. Rev. D, 68, 083506
Beers, T. C., Flynn, K., & Gebhardt, K., 1990, AJ, 100, 32
Beers, T. C., Forman, W., Huchra, J. P., Jones, C., & Gebhardt, K., 1991, AJ, 102, 1581
Benson, B. A., Church, S. E., Ade, P. A. R., Bock, J. J., Ganga, K. M., Henson, C. N., & Thompson, K. L., 2004, ApJ, 617, 829
Benson, B. A., et al., 2011, arXiv:1112.5435
Birkinshaw, M., Hughes, J. P., & Arnaud, K. A., 1991, ApJ, 379, 466
Birkinshaw, M., 1999, Phys. Rep., 310, 97
Biviano, A., & Girardi, M., 2003, ApJ, 585, 205
Biviano, A., & Katgert, P., 2004, A&A, 424, 779
Bonamente, M., Joy, M., LaRoque, S. J., Carlstrom, J. E., Nagai, D., & Marrone, D. P., 2008, ApJ, 675, 106
Book, L. G., & Benson, A. J., 2010, ApJ, 716, 810
Brodwin, M., et al., 2010, ApJ, 721, 90
Butcher, H., & Oemler, Jr., A., 1984, ApJ, 285, 426
Carlberg, R. G., Yee, H. K. C., & Ellingson, E., 1997, ApJ, 478, 462
Carlstrom, J. E., Holder, G. P., & Reese, E. D., 2002, ARA&A, 40, 643
Carlstrom, J. E., et al., 2009, arXiv:0907.4445
Colless, M., & Hewett, P., 1987, MNRAS, 224, 453
Coziol, R., Andernach, H., Caretta, C. A., Alamo-Martínez, K. A., & Tago, E., 2009, AJ, 137, 4795
Danese, L., De Zotti, G., & Di Tullio, G., 1980, A&A, 82, 322

Table 7
Clusters in the optical program not detected by ACT in the 2008 observing season.

Name	$N_{\rm gal}$	z	$S_{\rm BI}$ (km s^{-1})	r_{200c} (h_{70}^{-1} kpc)	M_{200c} ($10^{14}\,h_{70}^{-1}M_\odot$)
SCSO J0514–5126	15	0.73721 ± 0.00047	931 ± 154	1370 ± 218	6.3 ± 3.0
SCSO J0514–5140	22	0.73617 ± 0.00023	701 ± 125	1036 ± 182	2.7 ± 1.4
SCSO J0540–5614	17	0.44772 ± 0.00019	578 ± 115	990 ± 193	1.7 ± 1.0

da Silva, A. C., Kay, S. T., Liddle, A. R., & Thomas, P. A., 2004, MNRAS, 348, 1401
Dressler, A., & Shectman, S. A., 1988, AJ, 95, 985
Duffy, A. R., Schaye, J., Kay, S. T., & Dalla Vecchia, C., 2008, MNRAS, 390, L64
Evrard, A. E., et al., 2002, ApJ, 573, 7
Evrard, A. E., et al., 2008, ApJ, 672, 122
Fadda, D., et al., 1996, ApJ, 473, 670
Faltenbacher, A., & Diemand, J., 2006, MNRAS, 369, 1698
Fowler, J. W., et al., 2007, Appl. Opt., 46, 3444
Fowler, J. W., et al., 2010, ApJ, 722, 1148
Francis, M. R., Bean, R., & Kosowsky, A., 2005, JCAP, 12, 001
Girardi, M., Fadda, D., Giuricin, G., Mardirossian, F., Mezzetti, M., & Biviano, A., 1996, ApJ, 457, 61
Girardi, M., Escalera, E., Fadda, D., Giuricin, G., Mardirossian, F., & Mezzetti, M., 1997, ApJ, 482, 41
Grego, L., et al., 2001, ApJ, 552, 2
Hand, N., et al., 2011, ApJ, 736, 39
Hansen, S. M., Sheldon, E. S., Wechsler, R. H., & Koester, B. P., 2009, ApJ, 699, 1333
Hasselfield, M., et al., 2012, in prep.
Heisler, J., Tremaine, S., & Bahcall, J. N., 1985, ApJ, 298, 8
Hincks, A. D., et al., 2010, ApJS, 191, 423
High, F. W., et al., 2010, ApJ, 723, 1736
Hook, I., et al., 2004, PASP, 116, 425
Hughes, J. P., & Birkinshaw, M., 1998, ApJ, 501, 1
Jenkins, A., Frenk, C. S., White, S. D. M., Colberg, J. M., Cole, S., Evrard, A. E., Couchman, H. M. P., & Yoshida, N. 2001, MNRAS, 321, 372
Katgert, P., et al., 1996, A&A, 310, 8
Komatsu, E., et al., 2011, ApJS, 192, 18
Kurtz, M. J., & Mink, D. J., 1998, PASP, 110, 934
LaRoque, S. J., Bonamente, M., Carlstrom, J. E., Joy, M. E., Nagai, D., Reese, E. D., & Dawson, K. S., 2006, ApJ, 652, 917
Lin, Y.-T., & Mohr, J. J., 2004, ApJ, 617, 879
Mantz, A., Allen, S. W., Ebeling, H., Rapetti, D., & Drlica-Wagner, A. 2010a, MNRAS, 406, 1773
Mantz, A., Allen, S. W., & Rapetti, D., 2010b, MNRAS, 406, 1805
Mantz, A., Allen, S. W., Rapetti, D., & Ebeling, H., 2010c, MNRAS, 406, 1759
Marriage, T. A., et al., 2011a, ApJ, 737, 61
Marriage, T. A., et al., 2011b, ApJ, 731, 100
Marrone, D. P., et al., 2009, ApJ, 701, L114
Marrone, D. P., et al., 2011, arXiv:1107.5115
Melin, J.-B., Bartlett, J. G., Delabrouille, J., Arnaud, M., Piffaretti, R., & Pratt, W., 2011, A&A, 525, A139
Menanteau, F., & Hughes, J. P., 2009, ApJ, 694, L136
Menanteau, F., et al., 2010a, ApJS, 191, 340
Menanteau, F., et al., 2010b, ApJ, 723, 1523
Menanteau, F., et al., 2011, arXiv:1109.0953
Moore, B., Lake, G., Quinn, T., & Stadel, J., 1999, MNRAS, 304, 465
Motl, P. M., Hallman, E. J., Burns, J. O., & Norman, M. L., 2005, ApJ, 623, L63
Nagai, D., 2006, ApJ, 650, 538
Navarro, J. F., Frenk, C. S., & White, S. D. M., 1995, MNRAS, 275, 56
Oegerle, W. R., & Hill, J. M., 2001, AJ, 122, 2858
Pimbblet, K. A., Roseboom, I. G., & Doyle, M. T., 2006, MNRAS, 368, 651
Pinkney, J., Roettiger, K., Burns, J. O., & Bird, C. M., 1996, ApJS, 104, 36
Planck Collaboration, 2011a, A&A, 536, A8
Planck Collaboration, 2011b, A&A, 536, A10
Planck Collaboration, 2011c, A&A, 536, A12
Planck Collaboration, 2011d, A&A, 536, A9
Pratt, G. W., Croston, J. H., Arnaud, M., & Böhringer, H., 2009, A&A, 498, 361
Quintana, H., & Lawrie, D. G., 1982, AJ, 87, 1
Quintana, H., Carrasco, E. R., & Reisenegger, A., 2000, AJ, 120, 511
Reid, B. A., & Spergel, D. N., 2006, ApJ, 651, 643
Rines, K., Geller, M. J., & Diaferio, A., 2010, ApJ, 715, L180
Rozo, E., et al., 2010, ApJ, 708, 645
Schuecker, P., Böhringer, H., Reiprich, T. H., & Feretti, L., 2001, A&A, 378, 408
Sealfon, C., Verde, L., & Jimenez, R., 2006, ApJ, 649, 2006
Sehgal, N., Bode, P., Das, S., Hoyle, B., Hernández-Monteagudo, C., Huffenberger, K., Lin, Y., Ostriker, J. P., & Trac, H., 2010, ApJ, 709, 920
Sehgal, N., et al., 2011, ApJ, 732, 44
Shaw, L. D., Holder, G. P., & Bode, P., 2008, ApJ, 686, 206
Skibba, R. A., van den Bosch, F. C., Yang, X., More, S., Mo, H., & Fontanot, F., 2011, MNRAS, 410, 417
Springel, V., White, M., & Hernquist, L., 2001, ApJ, 549, 681
Springel, V., White, S. D. M., Tormen, G., & Kauffmann, G., 2001, MNRAS, 328, 726
Staniszewski, Z., et al., 2009, ApJ, 701, 32
Sunyaev, R. A., & Zel'dovich, Y. B., 1970, Ap&SS, 7, 20
Sunyaev, R. A., & Zel'dovich, Y. B., 1980, MNRAS, 190, 413
Swetz, D. S., et al., 2011, ApJS, 194, 41
Tauber, J. A., et al., 2010, A&A, 520, A1
Tinker, J., Kravtsov, A. V., Klypin, A., Abazajian, K. N., Warren, M., Yepes, G., Gottlöber, S., & van Speybroeck, L., 2008, ApJ, 688, 709
Tonry, J., & Davis, M., 1979, AJ, 84, 1511
Umetsu, K., et al., 2009, ApJ, 694, 1643
Vanderlinde, K., et al., 2010, ApJ, 722, 1180
van Dokkum, P., 2001, PASP, 113, 1420
Vikhlinin, A., et al., 2009, ApJ, 692, 1060
Voit, G. M., 2005, Rev. Mod. Phys., 77, 207
Werner, N., et al., 2007, A&A, 474, 707
Williamson, R., et al., 2011, ApJ, 738, 139
Yang, H.-Y. K., Bhattacharya, S., & Ricker, P. M., 2010, ApJ, 725, 1124
Zel'dovich, Y. B., & Sunyaev, R. A., 1969, Ap&SS, 4, 301

APPENDIX

ELECTRONIC DATA

Table 8 lists the properties of the BCGs for each of the ACT clusters (see Table 3). This table is an excerpt from the full table available online (from which the BCGs are shown for convenience), which contains all cluster members for the 16 ACT clusters. It is given for guidance in its form and content. Column 1 lists the adopted identification, based on the J2000.0 position of each galaxy and using the initials of the first three authors of this paper to identify the catalog. Columns 2 and 3 list the positions of the galaxies. Column 4 lists the magnitude in the i band; column 5 lists the cross-correlation redshifts and their associated errors as given by RVSAO. Column 6 lists the cross-correlation S/N r_{cc} and column 7 lists the main spectral features of each galaxy.

Table 8
Redshifts and magnitudes for the BCGs of the 16 ACT clusters

Identification	RA (hh:mm:ss)	Dec (dd:mm:ss)	m_i	z	r_{cc}	Main spectral features
SMH_J010257.7–491619.2	01:02:57.74	−49:16:19.2	19.186	0.87014 ± 0.00030	3.39	Ca-II K,H; [OII]
SMH_J021512.3–521225.3	02:15:12.26	−52:12:25.3	18.678	0.48587 ± 0.00016	3.90	Ca-II K,H
SMH_J023242.8–525722.3	02:32:42.80	−52:57:22.3	18.410	0.55592 ± 0.00014	4.53	Ca-II K,H
SMH_J023545.3–512105.2	02:35:45.28	−51:21:05.2	16.493	0.27825 ± 0.00015	7.18	Ca-II K,H
SMH_J023701.7–493810.0	02:37:01.71	−49:38:10.0	17.582	0.33554 ± 0.00016	10.42	Ca-II K,H
SMH_J030416.0–492126.3	03:04:16.04	−49:21:26.3	17.463	0.39289 ± 0.00020	9.43	Ca-II K,H
SMH_J033056.8–522813.7	03:30:56.83	−52:28:13.6	17.520	0.43969 ± 0.00019	10.23	Ca-II K,H
SMH_J034655.5–543854.8	03:46:55.49	−54:38:54.8	18.577	0.53107 ± 0.00013	6.16	Ca-II K,H
SMH_J043817.7–541920.7	04:38:17.70	−54:19:20.6	17.470	0.41955 ± 0.00012	9.42	Ca-II K,H
SMH_J050921.3–534212.2	05:09:21.38	−53:42:12.2	18.361	0.46257 ± 0.00022	7.53	Ca-II K,H; [OII]
SMH_J052114.5–510418.5	05:21:14.54	−51:04:18.6	19.060	0.67780 ± 0.00041	3.96	Ca-II K,H
SMH_J052805.3–525952.8	05:28:05.30	−52:59:52.8	19.715	0.76695 ± 0.00037	6.10	Ca-II K,H
SMH_J054637.6–534531.3	05:46:37.67	−53:45:31.3	21.184	1.06255 ± 0.00016	6.47	Ca-II K,H
SMH_J055943.2–524927.1	05:59:43.23	−52:49:27.1	19.103	0.61035 ± 0.00027	3.88	Ca-II K,H
SMH_J061634.1–522709.9	06:16:34.05	−52:27:09.9	18.594	0.68765 ± 0.00011	6.87	Ca-II K,H
SMH_J070704.7–552308.4	07:07:04.67	−55:23:08.4	16.754	0.29451 ± 0.00019	6.05	Ca-II K,H

Note. — BCGs of the 16 SZE-selected clusters presented here. This table is an extract from the full table provided in electronic form, which contains the data for the members of all clusters. It is provided for guidance on its form and content. Galaxies have been named based on their positions, and using the initials of the first three authors of this paper to identify the catalog.